



Eltes, F., Villarreal-Garcia, G. E., Caimi, D., Siegwart, H., Gentile, A. A., Hart, A. S., Stark, P., Marshall, G. D., Thompson, M. G., Barreto, J., Fompeyrine, J., & Abel, S. (2020). An integrated optical modulator operating at cryogenic temperatures. *Nature Materials*, 19, 1164-1168. <https://doi.org/10.1038/s41563-020-0725-5>

Peer reviewed version

Link to published version (if available):  
[10.1038/s41563-020-0725-5](https://doi.org/10.1038/s41563-020-0725-5)

[Link to publication record in Explore Bristol Research](#)  
PDF-document

This is the author accepted manuscript (AAM). The final published version (version of record) is available online via Nature Research at <https://www.nature.com/articles/s41563-020-0725-5> . Please refer to any applicable terms of use of the publisher.

## University of Bristol - Explore Bristol Research

### General rights

This document is made available in accordance with publisher policies. Please cite only the published version using the reference above. Full terms of use are available:  
<http://www.bristol.ac.uk/red/research-policy/pure/user-guides/ebr-terms/>

# An integrated optical modulator operating at cryogenic temperatures

Authors: Felix Eltes<sup>1,3</sup>, Gerardo E. Villarreal-Garcia<sup>2</sup>, Daniele Caimi<sup>1</sup>, Heinz Siegwart<sup>1</sup>, Antonio A. Gentile<sup>2</sup>, Andy Hart<sup>2</sup>, Pascal Stark<sup>1</sup>, Graham D. Marshall<sup>2</sup>, Mark G. Thompson<sup>2</sup>, Jorge Barreto<sup>2</sup>, Jean Fompeyrine<sup>1,3</sup>, Stefan Abel<sup>1,3</sup>

<sup>1</sup> IBM Research – Zurich, Säumerstrasse 4, 8803 Rüschlikon, Switzerland

<sup>2</sup> Quantum Engineering Technology Labs, H. H. Wills Physics Laboratory, University of Bristol, Bristol, BS8 1TL, United Kingdom

<sup>3</sup> Lumiphase AG, Brinerstrasse 21, 8003 Zürich, Switzerland (*current affiliation*)

**Integrated photonic circuits (PICs) operating at cryogenic temperatures are fundamental building blocks required to achieve scalable quantum computing, and cryogenic computing technologies<sup>1,2</sup>. Silicon PICs have matured for room temperature applications, but their cryogenic performance is limited by the absence of efficient low temperature electro-optic (EO) modulation. Here we demonstrate EO switching and modulation from room temperature down to 4 K by using the Pockels effect in integrated barium titanate (BaTiO<sub>3</sub>)-based devices<sup>3</sup>. We investigate the temperature-dependence of the nonlinear optical (NLO) properties of BaTiO<sub>3</sub>, showing an effective Pockels coefficient of 200 pm/V at 4 K. The fabricated devices exhibit an EO bandwidth of 30 GHz, ultra-low-power tuning which is 10<sup>9</sup> times more efficient than thermal tuning, and high-speed data modulation at 20 Gbps. Our results demonstrate a missing component for cryogenic PICs. Our results remove major roadblocks for the realisation of cryogenic-compatible systems in the field of quantum computing, supercomputing and sensing, and for interfacing those systems with instrumentation at room-temperature.**

Cryogenic technologies are becoming essential for future computing systems, a trend fuelled by the world-wide quest to develop quantum computing systems and future generations of high-performance classical computing systems<sup>4,5</sup>. While most computing architectures rely solely on electronic circuits, photonic components are becoming increasingly important (Supplementary Note, SN 1). First, PICs can be used for quantum computing approaches where the quantum nature of photons is exploited as qubits<sup>1,2</sup>. Second, optical interconnects can overcome limitations in

bandwidth and heat leakage that are present in conventional electrical interconnect solutions for digital data transfer between cryogenic processors and the room temperature environment<sup>6</sup> (SN 2). In addition, due to their low interaction with the environment, photons are the only viable carriers to transport quantum states over large distances. Optical interfaces are therefore essential for true quantum communication, necessary to connect multiple quantum computers<sup>7,8</sup> and for secure remote operation of quantum computers<sup>9</sup>. Recently, integrated photonics have also been exploited in quantum computing architectures based on trapped ion qubits<sup>10</sup>. The scalability of such a system is directly reliant on integrated cryogenic electro-optic modulators. The need for cryogenic photonics is not limited to computing systems, but covers a wide range of technical fields, such as radio astronomy<sup>11</sup>, particle physics<sup>12</sup>, and THz sensing<sup>13</sup>.

Today, the realisation of such photonic concepts is hindered by the lack of switches and modulators that operate at cryogenic temperatures with low-loss, high bandwidth, and low static power consumption. So far, only two concepts for cryogenic EO switches have been investigated, based either on the thermo-optic effect<sup>14</sup> or the plasma-dispersion effect<sup>15</sup>. Both mechanisms have physical limitations which intrinsically restrict the low-temperature performance of such devices. Thermo-optic phase shifters exploit Joule heating with large static power consumption and exhibit a bandwidth of less than a few MHz<sup>16</sup>. Plasma-dispersion-based devices require very high doping levels to compensate for carrier freeze-out at cryogenic temperatures and are intrinsically incapable of pure phase modulation. The high doping leads to large propagation losses and devices are limited to a bandwidth of <5 GHz in micro-disk modulators<sup>15</sup>. Both of these technologies are fundamentally limited from providing low-loss, low-power, high-speed switching and tuning as is fundamentally required for e.g. photonic quantum computing<sup>1,17</sup>. InP-on-Si modulators have also been explored for cryogenic use<sup>18</sup> but with limited performance and only to temperatures of 77 K, not reaching the few K or below as required by cryogenic applications.

The use of EO switches based on the Pockels effect has been shown to offer low propagation losses and high-bandwidth, combined with low static power consumption at room temperature<sup>3,19–21</sup>. While the Pockels effect has no intrinsic physical limitations for use at cryogenic temperature<sup>22</sup>, making a Pockels devices requires an integrated material which retains a large Pockels coefficient and which does not suffer from additional spurious effects at low temperature. No integrated cryogenic Pockels modulator has previously been reported, but room temperature devices have

recently been demonstrated using organics<sup>23</sup>,  $\text{PbZr}_x\text{Ti}_{1-x}\text{O}_3$ <sup>19</sup>,  $\text{LiNbO}_3$ <sup>20</sup>, and  $\text{BaTiO}_3$ <sup>3</sup>. Among them,  $\text{BaTiO}_3$  stands out due to having the largest Pockels coefficients<sup>3</sup> and exhibiting compatibility with advanced silicon photonics platforms<sup>24</sup>. We complete this triumvirate by demonstrating that  $\text{BaTiO}_3$  is also an ideal candidate for cryogenic EO integration.

Both the NLO properties and structural behaviour of  $\text{BaTiO}_3$  thin-films are entirely unknown at temperatures below 300 K. In fact, even in bulk  $\text{BaTiO}_3$  crystals the NLO behaviour below 270 K is not known, and the room temperature NLO behaviour of  $\text{BaTiO}_3$  thin-films has only recently been thoroughly investigated<sup>3</sup>. The phase transitions of thin-films are expected to differ from bulk crystals<sup>25</sup> due to the structural mismatch and thermal stress that exists between the substrate and the  $\text{BaTiO}_3$  layer<sup>26,27</sup>. They are entirely unknown for  $\text{BaTiO}_3$  on Si. Predictions of the Pockels tensor at cryogenic temperatures based on data at higher temperatures is not possible because in complex oxide materials the functional properties can change drastically with temperature. Here, we determine the cryogenic behaviour of  $\text{BaTiO}_3$  thin films by analysing the performance of  $\text{BaTiO}_3$ -based EO switches at temperatures down to 4 K. Our results show that efficient EO switching at cryogenic temperature is indeed possible and with bandwidths beyond 30 GHz. We also demonstrate the applicability of such devices for low-power switching and tuning as well as high-speed data modulation at 20 Gbps at 4 K.

In this work, we use two waveguide designs (Figure 1a) fabricated on single crystalline  $\text{BaTiO}_3$  layers bonded to  $\text{SiO}_2$ -buffered silicon substrates (see Methods). In the first design, silicon nitride (SiN)-based waveguides (Figure 1d) allowed us to study the pure NLO properties of  $\text{BaTiO}_3$  in absence of mobile charge carriers which could result in an additional, non-Pockels EO response. In the second, silicon (Si) waveguides served as more efficient devices (Figure 1e) to demonstrate high-speed data modulation. The enhanced efficiency originates from a larger optical-mode overlap with the  $\text{BaTiO}_3$  layer (41 %, Figure 1c) than with the SiN waveguides (18 %, Figure 1b). We found that the propagation losses (5.6 dB/cm, SiN device) were not affected by the presence of  $\text{BaTiO}_3$  in the active section (SN 3) throughout the temperature range studied.

To characterise the NLO behaviour of  $\text{BaTiO}_3$  at 4 K, we measured the induced resonance shift in a racetrack resonator as a function of the DC bias (Figure 1f), from which we determined the refractive index change of  $\text{BaTiO}_3$  ( $\Delta n_{\text{BTO}}$ ) as a function of the applied electric field (see Methods). This dependence allows us to study two of the three expected features of Pockels-based switching<sup>3</sup>:

NLO hysteresis and angular anisotropy, the third being the persistence of the Pockels effect at high frequencies ( $>10$  GHz)<sup>3</sup>.

The NLO response with a hysteretic behaviour (Figure 2a) indicates that a non-vanishing Pockels effect is preserved in BaTiO<sub>3</sub> down to a temperature of 4 K. We determine the effective Pockels coefficient,  $r_{\text{eff}}$ , by analysing the hysteretic behaviour of the refractive index change (SN 4). The dependence of  $r_{\text{eff}}$  on device orientation (Figure 2b) reveals the second signature of the Pockels effect, its anisotropy. The reduced magnitude at 4 K compared to room temperature is due to a temperature dependence of the Pockels effect, as discussed below. While  $r_{\text{eff}}$  is reduced with temperature, the EO response is expected to be present at high frequencies also at low temperature. Indeed, we observe a constant EO response in racetrack resonators with a low  $Q$  factor ( $Q \sim 1,800$ ) up to 30 GHz (Figure 2b). This constitutes the highest bandwidth for any cryogenic modulator reported to date. The frequency response is expected to remain flat at even higher frequency but could not be measured in our experiment (see Methods). The hysteretic behaviour, anisotropy, and high-speed response prove the presence of the Pockels effect in BaTiO<sub>3</sub> at 4 K.

We performed electrical characterisation of the material at low temperature using dedicated electrical test structures (SN 5). The resistivity of BaTiO<sub>3</sub> at 4 K is very high,  $>10^9 \Omega\text{m}$ . In fact, the measured current is dominated by capacitive charging and ferroelectric switching currents (Figure 2d). The field-dependent capacitance shows clear hysteretic characteristics (Figure 2e), consistent with ferroelectric domain switching.

The measured  $r_{\text{eff}}$  at 4 K is lower than at room temperature (Figure 2b), which has two causes. First, the Pockels effect itself is generally temperature dependent due to changes in strain and polarisation of the crystal<sup>28</sup>. Second, the non-zero elements of the Pockels tensor depend on the crystal symmetry, which can change abruptly with temperature due to structural phase transitions. BaTiO<sub>3</sub> bulk crystals are known to transition from a tetragonal phase at room temperature to orthorhombic and rhombohedral phases at lower temperatures ( $\sim 270$  K and  $\sim 200$  K respectively)<sup>25</sup>. Such transitions change the elements of the Pockels tensor and modify the magnitude of the effective Pockels coefficients<sup>28</sup>. Because phase transitions of thin-film materials can be drastically affected by substrate strain<sup>26,27,29</sup>, studying the properties of thin-film BaTiO<sub>3</sub> becomes critical when considering cryogenic applications. To investigate the effects of possible phase transitions, we measured  $r_{\text{eff}}$  in a range from 4 to 340 K. Indeed, the magnitude of  $r_{\text{eff}}$  is

strongly temperature-dependent (Figure 3). A peak around 240 K, with  $r_{\text{eff}} > 700$  pm/V, is consistent with the reported divergence of the  $r_{42}$  element of the Pockels tensor close to the tetragonal-orthorhombic transition<sup>28</sup>. Consistently, the permittivity of the BaTiO<sub>3</sub> layer (see Methods) also shows a peak in the same temperature range (SN 6), confirming that the abrupt change in  $r_{\text{eff}}$  is caused by a phase transition. Below 240 K the magnitude of  $r_{\text{eff}}$  decreases gradually to around 200 pm/V at 4 K. In addition to the phase transition at 240 K, a second phase transition occurs above 100 K causing a rapid change in  $r_{\text{eff}}$  of 90° devices. This phase transition is also observed in the qualitative behaviour of the NLO hysteresis which shows that the transitions is induced by the electric field (SN 6). While  $r_{\text{eff}}$  of BaTiO<sub>3</sub> is reduced at 4 K compared to room temperature, the value of ~200 pm/V is still larger than most other material systems at room temperature<sup>19,20</sup>. The effect of a reduced Pockels coefficient on the energy efficiency of EO switching is partially compensated for by a simultaneous reduction of the permittivity of BaTiO<sub>3</sub> (SN 6). Additionally, the conductivity of BaTiO<sub>3</sub> is reduced by more than four orders of magnitude (SN 5), resulting in a negligible static power consumption of BaTiO<sub>3</sub>-devices in cryogenic environments. No material instability or drift, as could for example be caused by pyroelectric effects, were observed at cryogenic or room temperature in any experiment.

We have reported the first ever measurement of the cryogenic NLO properties of BaTiO<sub>3</sub>, and indeed of any oxide thin-film material. The methods used to characterize these properties will enable further research to improve the cryogenic performance through engineering of the material properties<sup>29</sup>. However, already today we can use BaTiO<sub>3</sub> to demonstrate cryogenic devices with outstanding performance.

We demonstrate the applicability of BaTiO<sub>3</sub> for cryogenic photonic applications by two examples: low-power EO switching and high-speed data modulation. For switching we use a 500  $\mu\text{m}$  Mach-Zehnder interferometer with 2×2 multimode interference splitters, applying a voltage to one arm. Because the leakage current through BaTiO<sub>3</sub> at 4 K is 10<sup>4</sup> times lower than at 300 K, less than 10 pW static power is consumed when inducing a  $\pi$  phase shift to switch between the two optical outputs using an electric field of 6×10<sup>6</sup> V/m (Figure 4a,b), corresponding to a voltage of ~50 V in the given device geometry ( $V_{\pi}L = 5$  Vcm). Compared to state-of-the-art technology based on thermo-optic phase shifters<sup>14</sup>, static tuning using BaTiO<sub>3</sub> is one billion times more power efficient. The dynamic energy of the switch is ~30 pJ, which could be reduced to ~2 pJ, at a voltage of <5 V,

150 in an optimised device geometry (SN 7). Another important metric for EO switches is the losses  
151 in the device. Based on the measured propagation losses (5.6 dB/cm) and the device geometry we  
152 estimate an insertion loss of <1 dB (SN 3). The propagation losses are dominated by scattering  
153 losses in the SiN waveguide which can be reduced significantly by using a state-of-the-art  
154 fabrication process. SiN waveguides with propagation losses as low as 1 dB/m have been  
155 reported<sup>30</sup>.

156 As a second example, we performed data modulation experiments by sending a pseudo-random  
157 bit-sequence to a ring modulator ( $Q \sim 6'000$ ) fabricated with BaTiO<sub>3</sub>-Si waveguides and recording  
158 the optical eye-diagram (Figure 4c,d). Data transmission at rates up to 20 Gbps are achieved with  
159 our experimental setup using a drive voltage ( $V_{pp}$ ) of just 1.7 V, resulting in an extremely low  
160 energy consumption of 45 fJ/bit.

161 In conclusion, we have shown that BaTiO<sub>3</sub> thin films can be used to realise electro-optic switches  
162 and modulators for efficient cryogenic operation of silicon photonic integrated circuits. We have  
163 demonstrated low-power switching, as well as high-speed data modulation. Combining BaTiO<sub>3</sub>  
164 with silicon photonic integrated circuits, we make a building block available that was previously  
165 inaccessible for any cryogenic circuits. We anticipate that these components are a milestone for a  
166 versatile platform of cryogenic photonics for applications as diverse as quantum computing and  
167 communication<sup>1,8</sup>, astronomy<sup>11</sup>, fundamental physics<sup>12</sup>, and cryogenic sensing concepts<sup>13</sup>.

168

- 169 1. Silverstone, J. W., Bonneau, D., O'Brien, J. L. & Thompson, M. G. Silicon quantum  
170 photonics. *IEEE J. Sel. Top. Quantum Electron.* **22**, 6700113 (2016).
- 171 2. O'Brien, J. L., Furusawa, A. & Vučković, J. Photonic quantum technologies. *Nat. Photonics*  
172 **3**, 687–695 (2009).
- 173 3. Abel, S. *et al.* Large Pockels effect in micro- and nanostructured barium titanate integrated  
174 on silicon. *Nat. Mater.* **18**, 42–47 (2019).
- 175 4. Mukhanov, O. A. Energy-Efficient single flux quantum technology. *IEEE Trans. Appl.*  
176 *Supercond.* **21**, 760–769 (2011).
- 177 5. Ladd, T. D. *et al.* Quantum Computing. *Nature* **464**, 45–53 (2010).
- 178 6. Zeghbroeck, B. Van. Optical data communication between Josephson-junction circuits and  
179 room-temperature electronics. *IEEE Trans. Appl. Supercond.* **3**, 2881–2884 (1993).
- 180 7. Kimble, H. J. The quantum internet. *Nature* **453**, 1023 (2008).
- 181 8. Javerzac-Galy, C. *et al.* On-chip microwave-to-optical quantum coherent converter based on  
182 a superconducting resonator coupled to an electro-optic microresonator. *Phys. Rev. A* **94**,  
183 053815 (2016).
- 184 9. Greganti, C., Roehsner, M. C., Barz, S., Morimae, T. & Walther, P. Demonstration of  
185 measurement-only blind quantum computing. *New J. Phys.* **18**, 303–309 (2016).
- 186 10. Mehta, K. K. *et al.* Integrated optical addressing of an ion qubit. *Nat. Nanotechnol.* **11**, 1066  
187 (2016).
- 188 11. Johnston, A. R. *et al.* Optical links for cryogenic focal plane array readout. *Opt. Eng.* **33**,  
189 2013–2019 (1994).
- 190 12. Dowell, J. D. *et al.* Optoelectronic analogue signal transfer for LHC detectors. in  
191 *CERN/DRDC 91-41* (1991).
- 192 13. Benea-Chelmus, I.-C., Settembrini, F. F., Scalari, G. & Faist, J. Electric field correlation  
193 measurements on the electromagnetic vacuum state. *Nature* **568**, 202–206 (2019).
- 194 14. Elshaari, A. W., Zadeh, I. E., Jöns, K. D. & Zwiller, V. Thermo-Optic Characterization of  
195 Silicon Nitride Resonators for Cryogenic Photonic Circuits. *IEEE Photonics J.* **8**, (2016).
- 196 15. Gehl, M. *et al.* Operation of high-speed silicon photonic micro-disk modulators at cryogenic  
197 temperatures. *Optica* **4**, 374 (2017).
- 198 16. Harris, N. C. *et al.* Efficient, Compact and Low Loss Thermo-Optic Phase Shifter in Silicon.  
199 *Opt. Express* **22**, 83–85 (2014).
- 200 17. Li, Y., Humphreys, P. C., Mendoza, G. J. & Benjamin, S. C. Resource Costs for Fault-  
201 Tolerant Linear Optical Quantum Computing. *Phys. Rev. X* **5**, 41007 (2015).
- 202 18. Pintus, P. *et al.* Characterization of heterogeneous InP-on-Si optical modulators operating  
203 between 77 K and room temperature. *APL Photonics* **4**, 100805 (2019).



19. Alexander, K. *et al.* Nanophotonic Pockels modulators on a silicon nitride platform. *Nat. Commun.* **9**, 3444 (2018).
20. Wang, C. *et al.* Integrated lithium niobate electro-optic modulators operating at CMOS-compatible voltages. *Nature* **562**, 101–104 (2018).
21. Eltes, F. *et al.* Low-loss BaTiO<sub>3</sub>-Si waveguides for nonlinear integrated photonics. *ACS Photonics* **3**, 1698–1703 (2016).
22. Herzog, C., Poberaj, G. & Günter, P. Electro-optic behavior of lithium niobate at cryogenic temperatures. *Opt. Commun.* **281**, 793–796 (2008).
23. Lauermann, M. *et al.* 40 GBd 16QAM Signaling at 160 Gb/s in a Silicon-Organic Hybrid Modulator. *J. Light. Technol.* **33**, 1210–1216 (2015).
24. Eltes, F. *et al.* A BaTiO<sub>3</sub>-based electro-optic Pockels modulator monolithically integrated on an advanced silicon photonics platform. *J. Light. Technol.* **37**, 1456–1462 (2019).
25. Kay, H. F. & Vousden, P. XCV. Symmetry changes in barium titanate at low temperatures and their relation to its ferroelectric properties. *Lond. Edinb. Dublin Philos. Mag. J. Sci.* **40**, 1019–1040 (1949).
26. He, F. & Wells, B. O. Lattice strain in epitaxial BaTiO<sub>3</sub> thin films. *Appl. Phys. Lett.* **88**, 152908 (2006).
27. Tenne, D. A. *et al.* Absence of low-temperature phase transitions in epitaxial BaTiO<sub>3</sub> thin films. *Phys. Rev. B - Condens. Matter Mater. Phys.* **69**, 2–6 (2004).
28. Bernasconi, P., Zgonik, M. & Gunter, P. Temperature dependence and dispersion of electro-optic and elasto-optic effect in perovskite crystals. *J. Appl. Phys.* **78**, 2651–2658 (1995).
29. Acosta, M. *et al.* BaTiO<sub>3</sub>-based piezoelectrics: Fundamentals, current status, and perspectives. *Appl. Phys. Rev.* **4**, (2017).
30. Pfeiffer, M. H. P. *et al.* Ultra-smooth silicon nitride waveguides based on the Damascene reflow process: fabrication and loss origins. *Optica* **5**, 884–892 (2018).

## Acknowledgements

This work has received funding from the European Commission under grant agreements no. H2020-ICT-2015-25- 688579 (PHRESCO) and H2020-ICT-2017-1-780997 (plaCMOS), from the Swiss State Secretariat for Education, Research and Innovation under contract no. 15.0285 and 16.0001, from the Swiss National Foundation project no 200021\_159565 PADOMO, from EPSRC grants EP/L024020/1, EP/M013472/1, and EP/K033085/1, the UK EPSRC grant QuPIC (EP/N015126/1), and ERC grant 2014- STG 640079. JB thanks Dr. Döndü Sahin for her assistance with the experimental setup.

## Competing interests

F.E., J.F., and S.A. are involved in developing barium titanate technologies at Lumiphase AG. M.G.T. is involved in developing photonic quantum technologies at PsiQuantum Corporation.

## Data availability

The data that support the findings of this study are available from the corresponding authors upon reasonable request.

## Author contributions

F.E. and J.F. fabricated and structurally characterised the epitaxial BaTiO<sub>3</sub>/SrTiO<sub>3</sub> layer stack with support from H.S.. F.E designed all photonic circuits and fabricated them with support from D.C.. F.E., P.S. and S.A. performed optical simulations for the device design. G.E.V-G., F.E., A.A.G., A.H., G.D.M. and J.B. characterised the EO performance at different temperatures including low-speed and RF measurements. The EO data was analysed by F.E. and A.A.G.. F.E. and P.S. performed all electrical measurements. The concept for this work was defined by S.A., G.D.M. and M.G.T. and implemented by F.E. with support of S.A. and J.B.. F.E., J.F., and S.A. wrote the manuscript with contributions from all authors.

## Methods

**Device design and fabrication.** Single crystalline BaTiO<sub>3</sub> was deposited on top of an epitaxial 4-nm-thick SrTiO<sub>3</sub> seed layer by molecular beam epitaxy on 8" silicon-on-insulator (SOI) wafers with 220-nm-thick device silicon layer for SiN-based devices, and on 2" SOI wafers with 100-nm-thick device silicon for Si-based devices, following a process described elsewhere<sup>3</sup>. Direct wafer bonding was used to transfer the BaTiO<sub>3</sub> and device Si layers onto high-resistivity Si wafers capped with a 3-μm-thick thermal oxide. Specifics of the direct wafer bonding process can be found in ref. <sup>3</sup>.

For SiN-based waveguides the device Si layer was removed by dry etching, followed by chemical vapor deposition of SiN. The waveguide layer (Si or SiN) was patterned by dry etching. After waveguide patterning, a combination of SiO<sub>2</sub> cladding deposition, via etching, and metallisation was used to form the final cross-section. Intermediate annealing steps at 400°C under O<sub>2</sub> atmosphere were used to reduce propagation losses<sup>21</sup>.

The SiN-based waveguides use an 80-nm-thick BaTiO<sub>3</sub> layer, and 150-nm-thick SiN layer. The strip-waveguide width is 1.1 μm. The SiN thickness and waveguide width were chosen to ensure guiding of a single TE mode, and to maximize the overlap of that mode with the BaTiO<sub>3</sub> layer. The electrode-to-electrode gap is 9 μm to ensure no added losses caused by metal absorption. The racetrack resonators have a bend radius of 50 μm and straight sections of 75 μm length. The coupling gap (0.53 μm) between the access waveguide and the resonator was optimized for critical coupling.

The Si strip-waveguides were fabricated using 225-nm-thick BaTiO<sub>3</sub> and 100-nm-thick Si. The waveguide width is 0.75 μm. As for the SiN-based waveguides the waveguide dimension, including the Si thickness, were designed for TE single mode operation, with an optimized optical overlap with the 225-nm-thick BaTiO<sub>3</sub> layer. The racetrack resonator that was used has a bending radius of 15 μm and straight sections of 30 μm, and the electrode-to-electrode gap is 2.3 μm. The small electrode gap causes additional propagation losses in the resonator ensuring a Q-factor allowing >30 GHz bandwidth. The coupling gap of ~0.1 μm was optimized for critical coupling.

**Cryogenic measurements.** The cryogenic electro-optic measurements were performed in a Lakeshore CPX cryogenic probe station, fitted with RF (40 GHz BW, K-type connectors) and

optical feedthroughs. DC and RF signals were applied to the devices using RF probes, and optical coupling was achieved using a fibre array with polarisation maintaining fibres for 1550 nm. A tuneable laser (EXFO T100S-HP) and power meter were used to record transmission spectra (EXFO CT440). The cryogenic electrical measurements were performed in a Janis cryogenic probe station equipped with DC probes. Current-voltage and capacitance-voltage measurements were performed using a parameter analyser. Both cryogenic probe stations were cooled by liquid helium to a base temperature of 4.2 K.

**DC EO characterisation.** The DC electro-optic response was extracted by applying a voltage to the electrodes of a racetrack resonator and measuring the shift in resonance wavelength ( $\Delta\lambda$ ), compared to the unbiased case, as a function of the applied voltage. From the measured wavelength shift, the change in BaTiO<sub>3</sub> refractive index ( $\Delta n_{\text{BTO}}$ ) can be estimated as

$$\Delta n_{\text{BTO}} = \frac{\lambda_0 \cdot \Delta\lambda}{\text{FSR} \cdot L_{\text{E}} \cdot \Gamma_{\text{BTO}}}$$

where  $\Gamma_{\text{BTO}}$  is the optical confinement in BaTiO<sub>3</sub>, FSR is the free spectral range of the resonator,  $L_{\text{E}}$  is the electrode length, and  $\lambda_0$  is the resonance wavelength with no voltage.<sup>3</sup> The effective Pockels coefficient,  $r_{\text{eff}}$ , was then determined according to the procedure described in SN 4.

**RF frequency response.** To measure the EO frequency response (EO  $S_{21}$ ) a vector network analyser (VNA, Keysight PNA 50 GHz) was used to apply the electrical stimulus to a BaTiO<sub>3</sub> ring modulator. The modulated optical signal was applied to a photodiode (Newport 1024) and the response recorded by the VNA. Electrical calibration was performed before the measurement, and the response of the photodetector was compensated for the data analysis. While the VNA could generate signals up to 50 GHz, the bandwidth of the photodetector was 26 GHz, which in combination with large frequency-dependent electrical losses in the cryogenic probe station (SN 8) makes it impossible to measure the bandwidth beyond 30 GHz.

**Data modulation experiments.** For the data modulation experiment, a racetrack resonator modulator with a Si strip-waveguide was used. The electrical signal was generated using an arbitrary waveform generator. A pseudo-random bit stream of  $2^7-1$  bits was used for modulation. The electrical signal was pre-distorted to compensate for the finite time-response of the electrical signal path (SN 8). The signal was amplified using a RF amplifier and sent to the cryogenic setup, with an estimated voltage swing on the device of 1.7 V (SN 8). A Pritel FA-23 EDFA was used to

312    amplify the modulated optical signal which was applied to a photo diode and recorded on an  
313    oscilloscope.

314

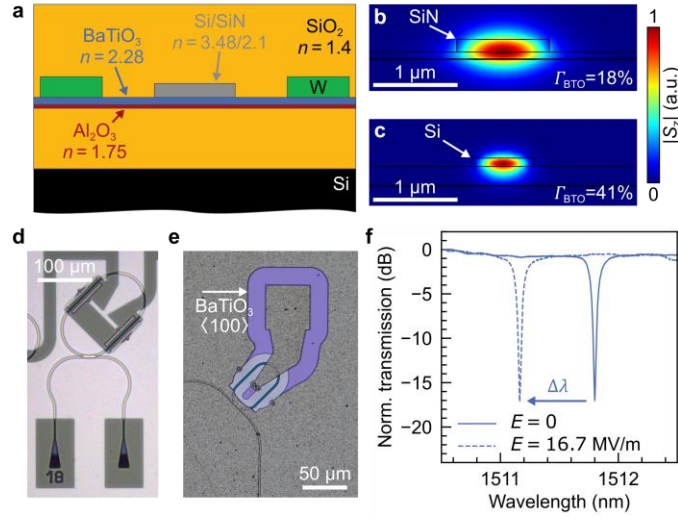


**Figure 1. BaTiO<sub>3</sub> electro-optic device concept.** **a**, Schematic cross-section of the devices. A silicon or silicon nitride layer forms a strip-waveguide (grey) on top of an BaTiO<sub>3</sub> layer (blue). A thin Al<sub>2</sub>O<sub>3</sub> layer (red) was used to improve adhesion (Methods). Lateral electrodes fabricated with W (green) are used to apply an electric field across the BaTiO<sub>3</sub>. The devices are embedded in SiO<sub>2</sub> (yellow) layers on top of silicon substrates (black). The refractive indices of BaTiO<sub>3</sub> and SiN were measured using spectroscopic ellipsometry. **b**, **c**, Simulations of the Pointing vector,  $|S_z|$ , of the transverse electric (TE) mode of the SiN waveguide geometry and the Si waveguide geometry, respectively. The two waveguide geometries show an optical confinement in BaTiO<sub>3</sub>,  $\Gamma_{\text{BTO}}$ , of 18 % and 41 %, respectively. **d**, **e**, Optical micrographs of BaTiO<sub>3</sub>-SiN and BaTiO<sub>3</sub>-Si racetrack resonators, respectively, used to characterise BaTiO<sub>3</sub> and demonstrate device functionality. The phase shifter section is embedded in the resonator which is evanescently coupled to access waveguides. The signal electrodes are connected to pads and the ground electrodes to a ground plane, for contacting using electrical probes. **f**, Characterisation principle of resonant electro-optic switches, showing example data of the shift in resonance wavelength between no applied field (solid line) and 16.7 MV/m (dashed line), which in this device corresponds to 150 V resulting in a shift of 4.3 pm/V. The shift in resonance wavelength,  $\Delta\lambda$ , is measured for an applied electric field and converted to the material properties of BaTiO<sub>3</sub> (see Methods).

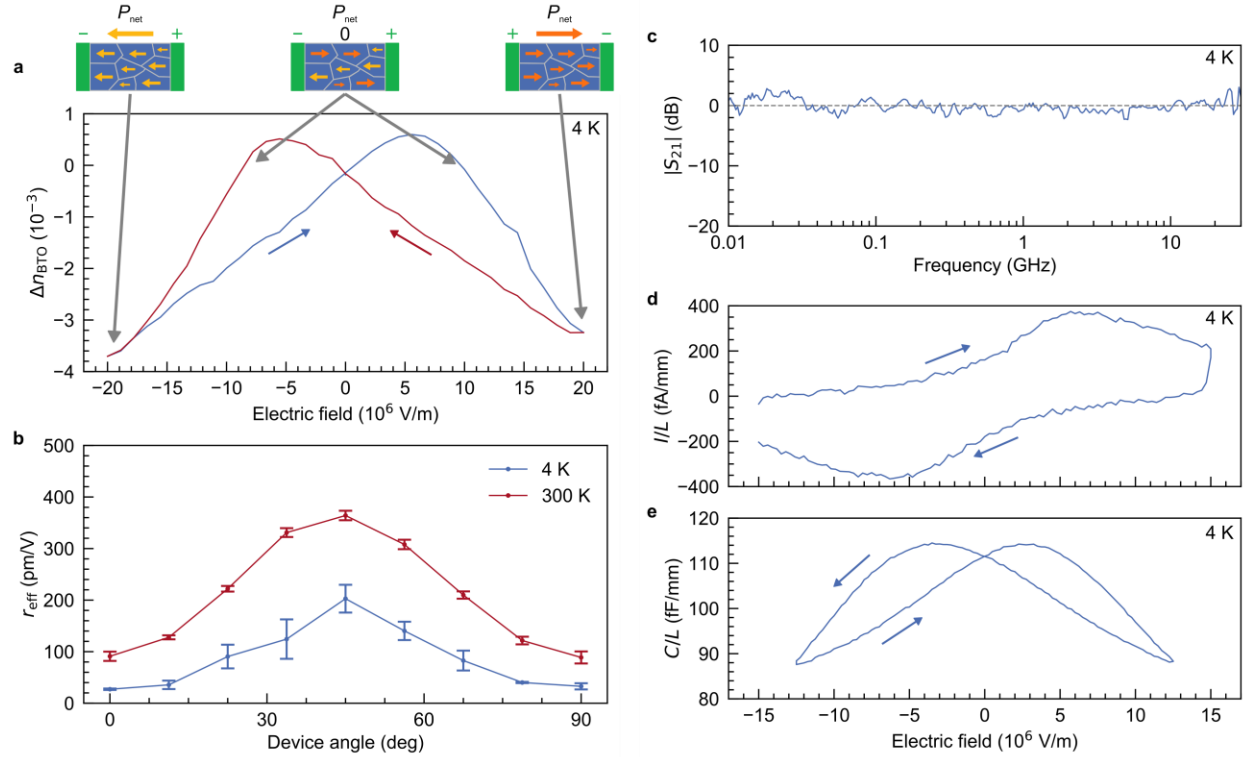


**Figure 2. Electro-optic and electrical response of BaTiO<sub>3</sub>-based optical switches at 4 K.** **a**, Refractive index change of BaTiO<sub>3</sub> as a function of applied electric field for a device in the 11.25° direction (as defined in **b**). The hysteretic behaviour between increasing (blue) and decreasing (red) voltage originates from ferroelectric domain switching in the BaTiO<sub>3</sub>, as illustrated schematically on top.  $P_{\text{net}}$  is the net polarization of all the domains. The arrows indicate the polarization of individual ferroelectric domains (blue) when a field is applied to lateral electrodes (green). **b**, Angular anisotropy of the effective Pockels coefficient in BaTiO<sub>3</sub> measured at 4 K and 300 K. The angle is defined relative to the BaTiO<sub>3</sub><100> direction. The same anisotropy as for BaTiO<sub>3</sub> at room temperature is observed but with reduced magnitude. The error bars show the combined standard error of the fit and from averaging measurements of multiple devices with the same orientation. **c**, Electro-optic  $S_{21}$ -parameter of BaTiO<sub>3</sub> ring resonator showing a flat response up to a frequency of 30 GHz at 4 K. The dashed line indicates 0 dB as a guide to the eye. **d**, Current measured as a function of electric field across the BaTiO<sub>3</sub> layer showing extremely low current flowing through the material. The current is dominated by capacitive charging, causing the offset between the sweep directions (indicated by the arrows), together with ferroelectric switching current resulting in the observed peaks (SN 5). **e**, Capacitance as a function of electric field, showing characteristic ferroelectric hysteresis and field-dependent permittivity.

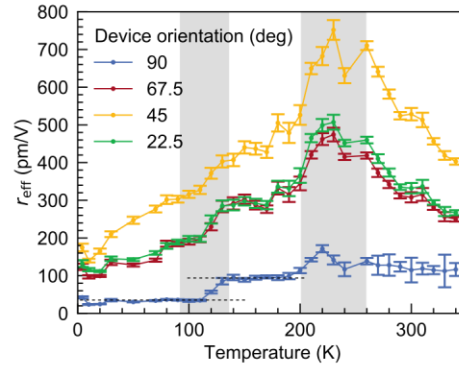


**Figure 3. Temperature dependence of the Pockels effect in BaTiO<sub>3</sub>.** The effective Pockels coefficient along different crystal orientations at temperatures from 4 K to 340 K. The peak around 240 K is the signature of a phase transition in BaTiO<sub>3</sub>. A second, field-induced phase transition occurs around 100 K, causing a sharp drop of  $r_{\text{eff}}$  in 90° devices (indicated by horizontal dashed lines). This phase transition is also evident in the qualitative evaluation of the optical response (SN 6). The grey areas indicate the temperature ranges of the respective phase transitions. The error bars show the standard error of the fit used to extract the Pockels coefficients (SN 4).



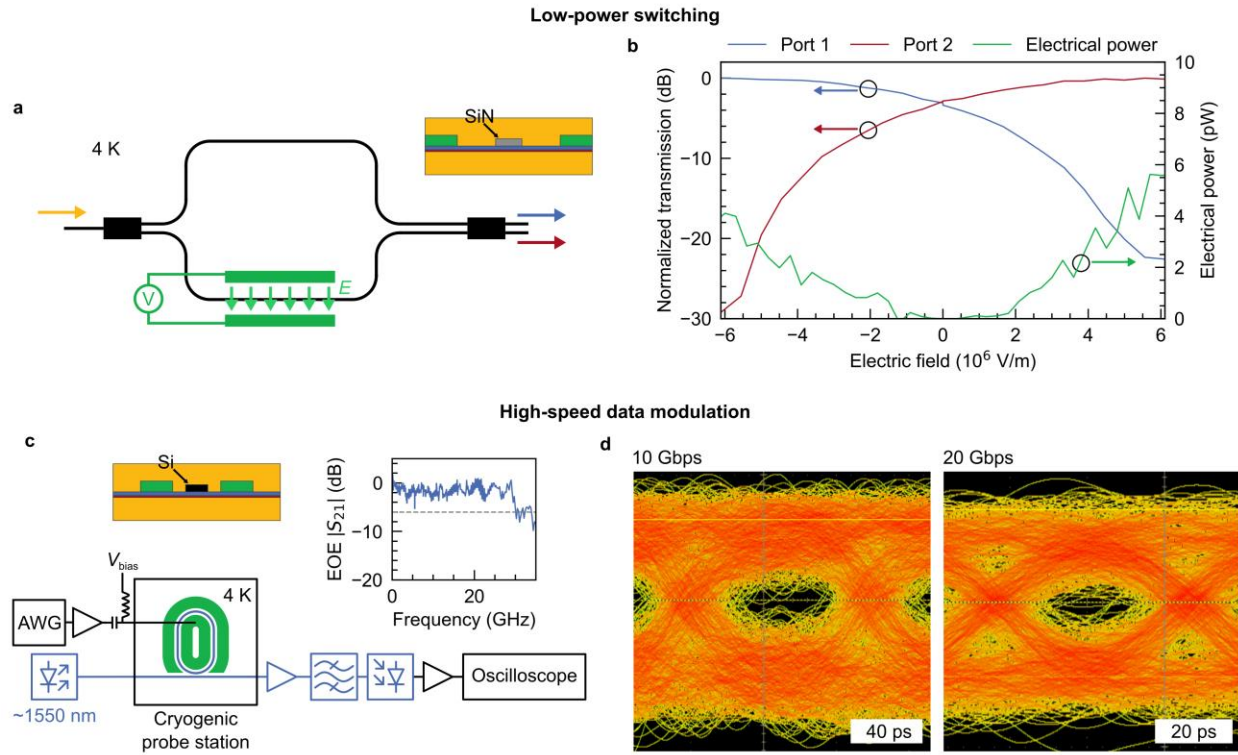


**Figure 4. Demonstration of low-power switching and high-speed data modulation with BaTiO<sub>3</sub>-based devices at 4 K.** **a**, Schematic of Mach-Zehnder (MZ) configuration used to switch between two ports. The yellow arrow indicates the input port and the red and blue arrows indicate output ports 1 and 2, respectively. Multi-mode interference splitters were used to split and combine the signal at the input and output ports. A voltage source,  $V$ , is used to apply an electric field,  $E$ , indicated by green arrows, across one arm of the MZ interferometer. The inset shows the waveguide cross-section. **b**, Transmission from both ports of a MZ switch as a function of applied electric field, along with the static power consumption. When fully switching between outputs, less than 10 pW static power is consumed, and only 30 pJ of dynamic energy. The field is kept below the coercive field of BaTiO<sub>3</sub> (SN 9) to exclude contributions from ferroelectric domain switching. **c**, Schematic of the experimental setup for data modulation. The data signal was generated using an arbitrary waveform generator (AWG) which was amplified and then combined with a bias voltage,  $V_{\text{bias}}$ , using a bias tee. A tuneable laser set to  $\sim 1550$  nm provided the optical carrier. After modulation in the cryogenic probe station, the optical signal was amplified by a fibre amplifier and filtered before being detected by a photodiode. The electrical signal from the photodiode was amplified and then recorded on a real-time oscilloscope. The left inset shows the waveguide cross-section and the right inset shows the electro-optic-electric (EOE) frequency response of the modulator. **d**, Eye diagrams recorded at 10 and 20 Gbps with  $V_{\text{pp}} = 1.7$  V, corresponding to modulation energy of 45 fJ/bit. The opening of the eyes is limited by noise from amplified spontaneous emission of the amplifier used in the experiment (SN 8).